

Article

Design of a Ventilated Façade Integrating a Luminescent Solar Concentrator Photovoltaic Panel

Giulio Mangherini ^{1,*}, Paolo Bernardoni ^{2,*}, Eleonora Baccega ³, Alfredo Andreoli ¹, Valentina Diolaiti ¹
and Donato Vincenzi ^{1,4}

¹ Department of Physics and Earth Sciences, University of Ferrara, 44122 Ferrara, FE, Italy; donato.vincenzi@unife.it (D.V.)

² Department of Chemical, Pharmaceutical and Agricultural Sciences, University of Ferrara, 44121 Ferrara, FE, Italy

³ Department of Architecture, University of Ferrara, 44121 Ferrara, FE, Italy

⁴ Consorzio Futuro in Ricerca, 44122 Ferrara, FE, Italy

* Correspondence: giulio.mangherini@unife.it (G.M.); paolo.bernardoni@unife.it (P.B.); Tel.: +39-0532-974270 (G.M.)

Abstract: The increasing trend towards decarbonization requires the reduction of the environmental impact of the building sector that currently accounts for approximately 40% of the total CO₂ emissions of European countries. Even though Luminescent Solar Concentrator (LSC) panels could be a very promising technology to be installed in urban environments, there is still little implementation of LSC panels in building façades. Here, the realization of a Ventilated Façade (VF) integrating an LSC device as an external pane is presented and a preliminary numerical and experimental investigation is used to evaluate the interaction between the different structure components. Thanks to the realization of a dedicated mock-up finite element method, models are calibrated and validated against experimental measurements, showing a good correspondence between simulated and measured data. Moreover, the electrical characterization of the LSC panel confirms that large area devices can be used as an external skin of VF, reporting a photovoltaic efficiency of 0.5%. The system's thermal and optical properties (estimated thanks to the software COMSOL Multiphysics) encourage the continuation of the research by considering different technologies for the VF internal skin, by scaling up the case study, and by running the simulation of an entire building considering winter and summer energy demands.

Keywords: building integrated photovoltaic; ventilated façade; luminescent solar concentrator; numerical modeling; semi-transparent photovoltaic panel; thermal simulation



Citation: Mangherini, G.; Bernardoni, P.; Baccega, E.; Andreoli, A.; Diolaiti, V.; Vincenzi, D. Design of a Ventilated Façade Integrating a Luminescent Solar Concentrator Photovoltaic Panel. *Sustainability* **2023**, *15*, 9146. <https://doi.org/10.3390/su15129146>

Academic Editors: Yuanda Cheng, Abdulaziz Banawi and Yao Yu

Received: 3 April 2023

Revised: 22 May 2023

Accepted: 1 June 2023

Published: 6 June 2023



Copyright: © 2023 by the authors. Licensee MDPI, Basel, Switzerland. This article is an open access article distributed under the terms and conditions of the Creative Commons Attribution (CC BY) license (<https://creativecommons.org/licenses/by/4.0/>).

1. Introduction

The reduction of carbon dioxide emissions related to building operations will be one of the crucial steps towards achieving global carbon neutrality [1]. Densely populated areas (in particular commercial buildings) are the core contributors to building energy consumption and emissions [2]. The tailored implementation of Building Integrated PhotoVoltaic (BIPV) solutions has the potential to highly increase the overall building energy efficiency [3–5] while improving the quality of life under multiple aspects [6,7], especially if a more rational use of energy is implemented [8–10]. Considering the wide-range of BIPV technologies, their tailored implementation has the potential to improve the quality of human life under multiple prospects [6,7]. A particularly interesting BIPV application is the implementation of PV technologies in Double Skin Façades (DSFs) [11,12] or Ventilated Façades (VFs) [13], since, as identified by De Boeck et al. [14], an improvement in the insulation efficiency of the building envelope is a key parameter to increasing its energy performance. In this regard, DSFs and VFs have been identified as one of the best options to reduce building

energy loads [15], as their architectural flexibility allows the interaction between outdoor and indoor spaces to be modified according to the building needs [16].

A DSF is composed of two panes, commonly called skins, separated by a cavity [17], having a different width according to several parameters (namely the design concepts), the presence of shading devices or vegetation, or the necessity to guarantee access to the cavity interior [18,19]. These structures normally maximize their performance by having low transmittance glasses or opaque panes as an external skin [20].

Indeed, for the cavity width, the optical properties of both internal and external layers may vary depending on the nature of the pane employed as the skin (e.g., glass, concrete, or PV devices), thus different façades may range from highly transparent [21,22] to completely opaque [23,24]. The working principle of a VF lies in the harvesting of solar radiation to create a thermal gradient between the outer and inner pane, which heats the air inside the cavity, creating the buoyancy phenomenon [25]. The air cavity may act as a ventilation channel (if the buoyancy effect is used to regulate the temperature of the indoor spaces) or as a buffer zone (if the air acts as an additional insulation layer) [17]. Narrow cavities are preferred for reducing the building cooling load, as the channel tightness increases the stack effect and leads to a more effective extraction of air through the cavity. On the other hand, larger cavities are preferred when the DSFs are primarily employed as a buffer zone or to increase the heat transfer towards the interior rooms [26].

The review work conducted by Quesada et al. [27,28] testifies that the implementation of photovoltaic or photovoltaic-thermal panels as façade components can guarantee the production of a considerable amount of energy, also thanks to the cooling effect of the air cavity circulating behind the modules. However, the implementation of standard flat PV modules in urban environments has three main drawbacks. The first drawback is their architectonic impact, because, to maximize their efficiency, solar panels are usually characterized by dark surfaces [29]; however, each attempt to increase their architectonic impact highly affects their efficiency [30–32]. The second criticality is given by their tolerance to shading, since the presence of surrounding buildings, streetlights, or trees may generate steep and localized shaded regions on the panels, which, besides power output reduction, can lead to permanent damage if bypass diodes are not properly installed [33]. The last drawback is represented by the dominant radiation in the urban context, as the heterogeneity of the environment causes diffuse solar radiation to dominate over direct radiation, under which standard flat solar panels guarantee their best performance [34].

In this context, the implementation of a Luminescent Solar Concentrator (LSC) as an external skin of a VF can be a promising solution to overcome the abovementioned criticalities. A typical LSC panel is composed of a transparent glass or plastic slab that is functionalized with active luminophores, which can be classified into three main categories: organic compounds [35], metalorganic complexes [36], and quantum dots [37]. The fluorophores absorb part of the radiation that impinges on the slab and then re-emit it at a longer wavelength. The fluorescence radiation can be either confined inside the slab, thanks to total external reflection, or can be transmitted. The installation of PV cells along the slab edges ensures the creation of a proper LSC PV panel (see Figure 1), reducing the number of solar cells for an active area. The presence of the slab acting as a wave guide allows the LSC panels to harvest (with a similar efficiency) both direct and diffuse solar radiation, thus ensuring a higher tolerance to shading and hotspots with respect to standard PV devices [38]. Furthermore, the luminophores realize a down-shifting of wavelengths that cross the slab, thus exposing the solar cells to a wavelength spectrum in which their external quantum efficiency is higher [39,40].

Thanks to their optical properties, LSC panels are particularly indicated for integration in urban environments, even if their high transparency leads to a lower photovoltaic efficiency when compared with the traditional BIPV systems. For this reason, works concerning the development of LSC devices are often limited to their integration in semi-transparent surfaces such as PV windows. However, research on large-area LSC panels has testified that, although their power production is limited, if the system is properly designed,

they may manage to support the modification of the air channel configuration [41,42]. Their transparency allows the coupling with any type of internal skin, presenting a customizable design and thus ensuring the most efficient solar radiation harvest throughout the whole year, while, at the same time, tailoring the building envelope according to the desired exterior architectural appearance [43]. The absence of clearly visible solar cells on the outer skin is appreciable in many respects and LSCs are one of the few large-area solar technologies that present this feature. Considering the literature absence of an in-depth analysis of a VF integrating an LSC panel as an external skin, this research focuses on the development of a mock-up that represents one of the modules that can be integrated in a building scale façade.

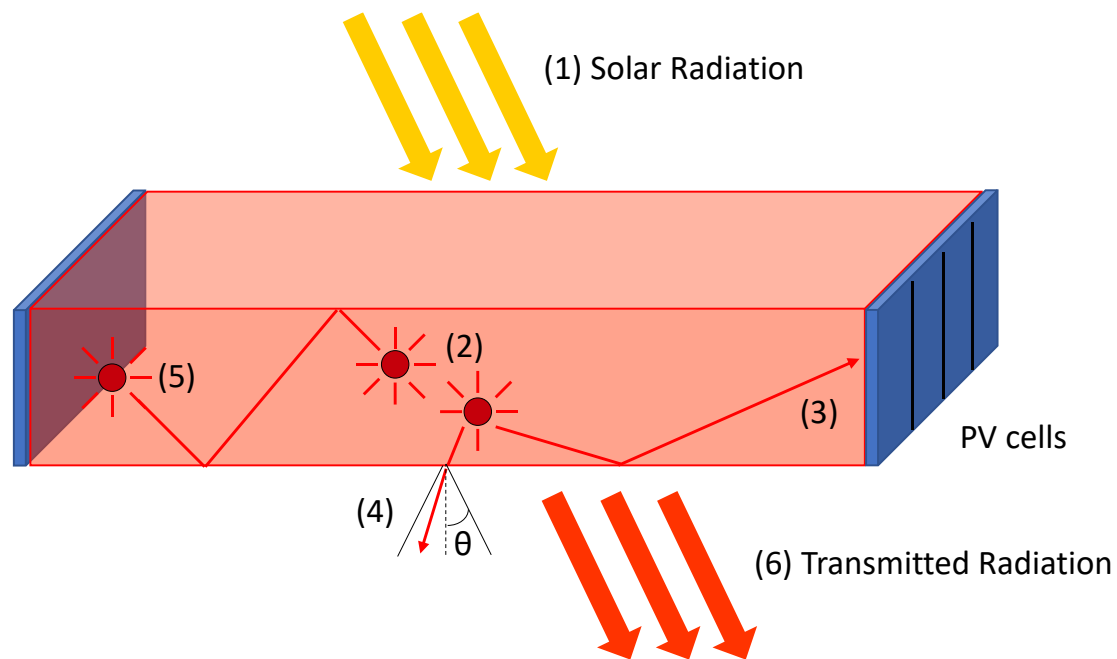


Figure 1. Model that schematizes the working principle of an LSC panel by highlighting the main phenomena: (1) impinging solar radiation, (2) light emitted by the luminophores, (3) fluorescence light reaching the slab edges (PV cells) thanks to total internal reflection, (5) fluorescence radiation that is absorbed by another dye molecule (self-absorption), (6) transmitted radiation, and (4) fluorescent light subjected to escape cone losses. The percentage of emitted light confined inside the slab depends on the flatness of the slab surface and on the difference in refractive index between the slab and the air (according to Snell's law).

The research presented in this work aims to develop the integration of an LSC panel as an external skin of a natural VF, as, for this system, the high transparency of LSC panels ensures the increase in solar radiation that reaches the internal skin when compared with traditional solar panels. In order to estimate the system's physical properties, as well as the interaction between the VF components, two data acquisition campaigns are performed thanks to the realization of a dedicated mock-up, which allows modification of the cavity configuration. This system is also modeled via a Finite Element Method (FEM) software called COMSOL Multiphysics (V5.6) [44], which, according to [45], was chosen from a multitude of other software as it allows the implementation and the coupling of different physical phenomena, which is mandatory to properly describe the air flow inside the cavity of the set-up proposed here. Firstly, the Closed Façade Model (CFM) is developed to calibrate the system's physical properties through the comparison with experimental data. Then, the Open Façade Model (OFM) (that implements the same thermal and optical properties inserted into the CFM) is used to validate the system's physical parameters.

2. Materials and Methods

2.1. Façade Mock-Up

In order to calibrate the models developed in COMSOL by using experimental data, a mock-up of the VF, having an overall volume of $0.5 \times 0.3 \times 1 \text{ m}^3$, was built in the Ferrara University campus. It was a small wall sample, where the proper VF was realized by combining, in order, the LSC panel, the air cavity, the Al panel, and the insulating layer (made of Expanded Polystyrene (XPS)), whereas the last layer, made of hollow bricks, was added to increase the system's thermal inertia. All the mock-up layers were 0.5 m large and 1 m high but with different widths, which, from the outer to the inner layer, were 0.005 m (LSC panel), 0.003 m (Al pane), 0.055 m (XPS), and 0.12 m (hollow bricks).

For structural and insulation support, both the insulating and the bricks layers were inserted into a wooden framework covered with additional insulating material, thus decreasing the heat dispersion along the longitudinal directions and ensuring a mono-dimensional heat transfer perpendicular to all the layers. The same insulating material was also used to modify the air cavity flow conditions, changing from a closed- to an open-channel configuration. Thanks to two additional edges, the wooden framework was also used as an anchoring point for the LSC panels and as lateral boundaries of the air channel. A schematic representation is shown in Figure 2. The temperature of the mock-up was monitored by installing several Negative Temperature Coefficient (NTC) thermistors between the different layers, which ensured an excellent long-term stability and a high sensitivity over the temperature range in which the measurements were performed. Overall, a matrix of $5 \times 5 \times 3$ NTC sensors were installed; this distribution allowed to organize the thermistors according to two subdivisions. The first one consisted of the subdivision of the main matrix in three 5×5 matrices that crossed all five mock-up layers generating three different identical cross-sections of the mock-up. The second was represented by the splitting of the initial distribution in five longitudinal 5×3 sub matrices involving just one material layer. Level 1 corresponded to the NTC installed behind the bricks, Level 2 to the one between the insulation material and the bricks, and Level 3 to the sensors within the insulation layer. Level 4 and Level 5 referred to sensors installed on the façade skins and, in particular, Level 4 identified the NTCs on the aluminum pane, whereas Level 5 to the ones coupled to the internal side of the LSC panel. For each longitudinal matrix, the position and the spacing between the sensor was constant; specifically, the first rows were placed at 0.085 m from the mock-up base with each row and each column spaced by 0.20 m and 0.125 m, respectively.

Figure 3 shows the mock-up with the disposition of three thermistor levels: 5, 4, and 1, respectively. Moreover, a seventy-sixth NTC was used for ambient temperature monitoring. Data were acquired by using the Multi_IO system, a modular network of electronic boards designed within the Sensors and Semiconductors Laboratory of the University of Ferrara. This system was developed to handle digital and analog input and output given by environmental sensors such as the Global Normal Irradiance (GNI) impinging on the mock-up, the wind direction and velocity, or by the NTC sensors. A more detailed description of the Multi_IO system is reported in the Supporting Information (SI).

LSC Panel Assembly

The wave guide of the LSC panel was a PolyMethylMethAcrylate (PMMA) slab functionalized with 160 ppm of an organic dye developed by BASF Corporation (termed Lumogen® Red 305). This fluorophore was chosen as it is one of the most efficient organic dyes and as its price per kilogram ensured a competitive price-to-watt ratio when compared with other semi-transparent PV technologies [38].

The proper LSC panel was assembled by mounting four PV arrays along each of the slab's longer edges by using an optical UV glue [46]. The receivers could, in principle, be connected in series or in parallel, depending on the context in which the panel should be integrated. The arrays mounted on the same edge were connected in series and, to minimize the possible mismatch caused by direct exposure of the cells to sunlight (specifically in the

morning and evening), the two PV branches were connected in parallel. Each of the eight arrays was manufactured by soldering to $24.6 \times 1.2 \text{ cm}^2$ printed circuit board ten back contact SunPower™ C50 solar cells [39], which were previously cut into rectangles (with an area of $2.4 \times 0.8 \text{ cm}^2$). The results presented in [38] led to the covering of the LSC shorter edges with a high-efficiency dielectric mirror film [47]. The mechanical coupling between the LSC panel and the whole structure was carried out by encasing the module in an aluminum frame; the electrical connections took place through two wires coming out of the aluminum casing. To prevent a possible efficiency reduction due to all the manufacturing processes (namely an increase of the escape cone losses due to the interface between the slab surface and the assembly materials (i.e., UV glue, aluminum frame)), a 5 mm strip of reflective film was also added to the faces of the slabs next to the PV cells.

Position of the NTC temperature sensors:

- Level 1: on the back of the brick layer
- Level 2: between the insulation and the brick layer
- Level 3: between the two insulation panels
- Level 4: on top of the aluminum plate
- Level 5: on the back of the LSC panel

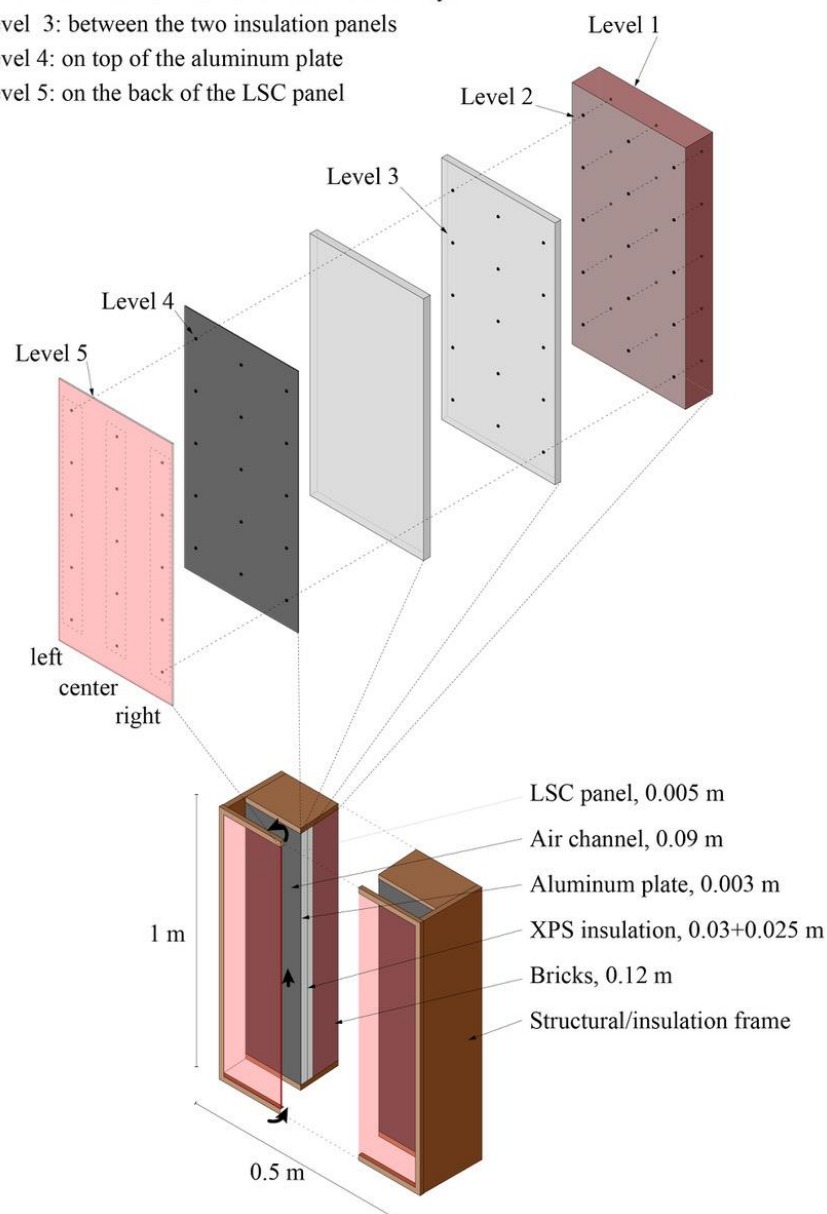


Figure 2. Axonometric view of the mock-up installed in the Ferrara University campus, where, in the top part, the position of the installed temperature sensors (black dots) and their subdivision in levels (1–5) and sections (left/central/right) is highlighted.

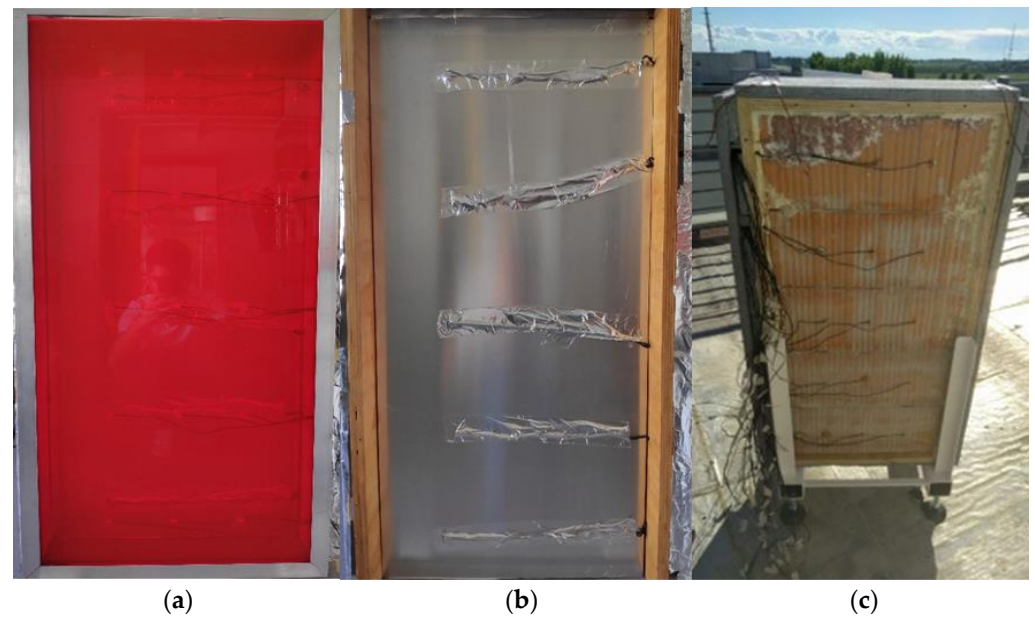


Figure 3. Pictures of different mock-up physical layers also presenting NTC: (a) Level 5, (b) Level 4, and (c) Level 1. The back of the mock-up was further insulated during the data acquisition campaigns.

2.2. FEM Models

COMSOL Multiphysics is a software that allows the simulation of physical systems by using a tree structure subdivided into several nodes and branches, whose numbers are related to the complexity of the modeled physical system. The simulation was implemented via a 2D model, in which the different layers composing the mock-up were simulated thanks to geometrical entities (domains) having time-varying boundary conditions. The model developed in COMSOL allowed to study the temperature distribution in the whole façade by solving the following equations:

$$\rho c_p \frac{\partial T}{\partial t} + \rho c_p \mathbf{u} \cdot \nabla T + \nabla \cdot (-k \nabla T) = q, \quad (1)$$

$$\rho \frac{\partial \mathbf{u}}{\partial t} + \rho (\mathbf{u} \cdot \nabla) \mathbf{u} = \nabla \cdot (-p \mathbf{I} + \mathbf{K}) + \mathbf{F} + \rho \mathbf{g}, \quad (2)$$

$$\frac{\partial \rho}{\partial t} + \nabla \cdot (\rho \mathbf{u}) = 0, \quad (3)$$

$$q = F_{view}(G - J), \quad (4)$$

where the bolded components identify vector quantities; ρ is the material density; c_p its heat capacity at constant pressure; T is the absolute temperature expressed in [K]; \mathbf{u} is the material velocity vector, which is considered different from zero only for the domains defined as fluid. The term $-k \nabla T$ accounts for the conductive heat flux; it is defined as the product between the material thermal conductivity, k , and the temperature gradient, ∇T . $-p \mathbf{I} + \mathbf{K}$ represents the Cauchy stress tensor and accounts for pressure and viscous stress. $\rho \mathbf{g}$ models the gravity force, whereas \mathbf{F} is the vector that simulates additional volumetric forces. F_{view} models the surface view factor, G is the total radiation impinging on that surface, and J its radiosity, defined as the total radiation that exits from the surface. Finally, q is the net heat flux entering ($q > 0$) or exiting ($q < 0$) the selected surface.

These equations are related to specific nodes called physics that model the physical phenomena considered in the simulation. In particular, Equation (1) is solved by the “Heat transfer in solid and Fluids” (HT) node, which models the conduction phenomena, whereas Equations (2) and (3) are handled by the “Laminar Flow” (SPF) physics, which models the fluid dynamic aspects in the façade cavity. The flow nature (laminar or turbulent) was

verified according to the official COMSOL procedure presented by F. Schlegel [48], which, considering the assumptions made within this work, led to a Grashof number of the order of 1.5×10^6 , thus confirming the laminar flow hypothesis.

The thermal properties attributed to each system component were initially attributed by using data available in the literature [49–54] and then adjusted in order to better match the experimental and the numerical results.

Finally, Equation (4) is introduced by the “Surface-to-surface Radiation” (RAD) interface, modeling the radiative phenomena between surfaces.

To correctly simulate the whole system, COMSOL requires the definition of some parameters that resemble the physical properties of the desired elements; the properties considered mandatory for the model are subordinated to the physics implemented in the simulation. HT and SPF physics require the bulk properties needed to solve Equations (1)–(3), such as material thermal conductivity, λ , its density ρ , its heat capacity at constant pressure C_p , or its dynamic viscosity μ . Moreover, the SPF node demands that the objects inserted in it are also defined as “Fluid” in the HT physic.

The distinction between “Solid” and “Fluid” also affects the domain’s optical properties; in fact, COMSOL considers the former as opaque, namely with a bulk transmissivity equal to 0%, and the latter as transparent, associating them with a bulk transmissivity equal to 100%. Being RAD a physics that involve only surfaces, the parameters needed to solve Equation (4) are the surface emissivity ε , transmissivity τ , and reflectivity ρ .

However, it is important to underline that the definition of the surface properties depend on different simulation aspects such as the methodology used to model the radiation, the type of surface, and the imposed boundary. The surfaces inserted in the RAD interface were modeled following the COMSOL application Greenhouse Effect [55], according to which all the surfaces were modeled as diffusive surfaces. Specifically, each surface was subjected to the following equations:

$$J_i = \varepsilon_i \varepsilon_b(T) FEP_i(T) + \rho_{d,i} G_i, \quad (5)$$

$$\varepsilon_i + \rho_{d,i} = 1, \quad (6)$$

$$q_{r,net,i} = \varepsilon_i (G_i - \varepsilon_b(T) FEP_i(T)), \quad (7)$$

where (as in Equation (4)) J_i is the surface radiosity, ε_i and $\rho_{d,i}$ are the surface emissivity and diffuse reflectivity, $\varepsilon_b(T)$ is the blackbody radiation emission, and $q_{r,net,i}$ defines the total radiative heat flux entering the surface. G_i is the total radiation impinging on the surface and it can be better defined by Equation (8):

$$G_i = G_{m,i}(J_i) + F_{amb,i} \varepsilon_{amb,i} \varepsilon_b(T_{amb}) FEP_i(T_{amb}) + G_{ext,i}, \quad (8)$$

where $G_{m,i}$ is the mutual radiation between different surfaces, $\varepsilon_{amb,i}$ is the ambient emissivity, and $G_{ext,i}$ is the external irradiation. $F_{amb,i}$ is the ambient view factor, which is considered equal to 1 for all the developed models. The subscript i refers to the considered wavelength range; its presence is due to the choice of the multiple spectral bands option. This option allows the splitting of the modeled radiation into different wavelength ranges, having a weight with respect to the totality of the simulated ranges determined by the $FEP_i(T)$. From Equation (6), it can be noticed that diffusive surfaces do not model surface transmittance, as, by definition, they absorb or reflect the impinging light.

With the exception of the wavelengths reported in Figure 4, the values of the LSC and Al emissivity, ε_{LSC} and ε_{Al} , are attributed starting from the literature evidence [56–60] and then adjusted to better match the experimental data. The direct estimation of the material emissivity within the range 350–800 nm is particularly important for the model development, as the LSC panel optical properties in the visible-NIR spectrum highly depend on the manufacturing process, i.e., the slab material or the fluorophore concentration.

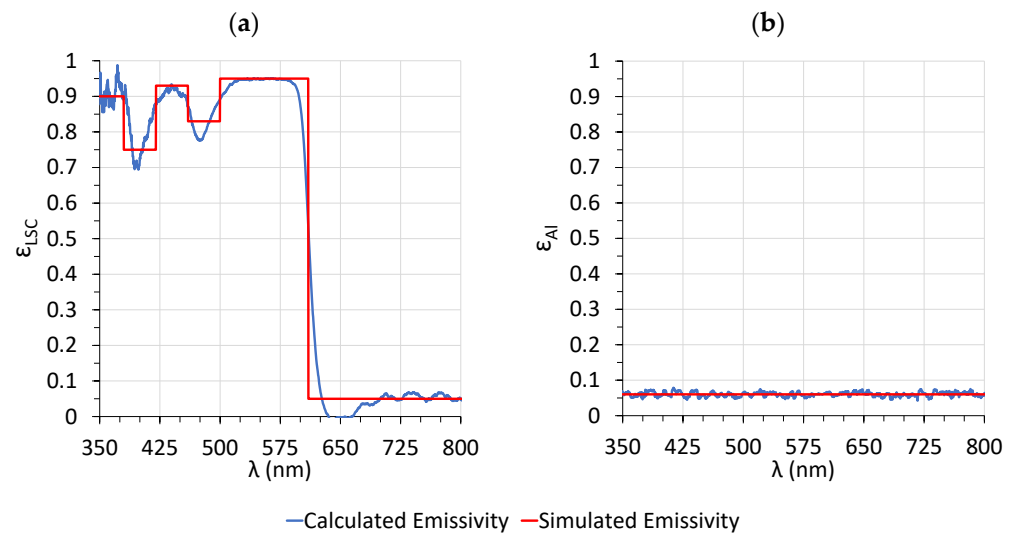


Figure 4. (a) LSC and (b) aluminum emissivity calculated spectrum in the range 350–800 nm (blue solid lines) and functions defined in COMSOL modeling the material emissivity (red solid lines).

Being RAD a physics that models radiative exchange between surfaces, the LSC and absorber optical bulk properties are modeled thanks to the opacity parameters $LSC_{Opacity}$ and $Al_{Opacity}$. This parameter defines whether the bulk domain absorbs or transmits the impinging radiation; the LSC is defined as Opaque (OP) for the wavelengths shorter than $0.610 \mu\text{m}$ and Transparent (TR) for the longer ones, whereas the Al pane is defined as OP for all the considered ranges. The ambient emissivity parameter, ϵ_{amb} , is inserted to better approximate the VF cooling due to the long wave radiation exchange between the system and the sky; its functional expression is defined considering that the infrared radiation emitted by buildings could be split into two ranges. The first range is associated to an ambient emissivity near to 1 and is the one in which the infrared radiation is absorbed by the water vapor and other greenhouse gases. The second range corresponds to the long-wave radiation emitted in the so-called atmospheric window ($8\text{--}13 \mu\text{m}$), a spectral range in which the atmosphere is almost transparent.

Normally, building simulation tools model these interactions by introducing two different temperatures: a temperature called T_{sky} and the ambient temperature T_{amb} . They are both used to model the building radiative heat exchange with the ambient; the former is employed for the heat exchange within the atmospheric window, whereas the latter is employed for the remaining wavelength ranges [61,62]. However, not being a COMSOL building simulation tool, it considers only one temperature T_{amb} and the only way to improve the accuracy of the atmospheric window effects is to modify the value of the ambient emissivity [63].

Irrespective of the model, the convective heat exchange between the ambient and the LSC external surface is inserted in the HT interface and is computed according to Equation (9), where the convective heat transfer coefficient h is defined by Equation (10) [64]:

$$q = h(T_{ext} - T) \quad (9)$$

$$h = 5.7 + 3.8 \cdot v_{wind} \quad (10)$$

where h is the convective heat transfer coefficient and v_{wind} is the wind velocity.


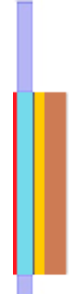
2.3. Model Domains

The unidirectionality of heat fluxes, achieved thanks to the insulating and structural frame installed in the mock-up, supported by the results presented by Pasut and De Clari [65], allowed the development of 2D simulation models. In each of these models, a cross section of the whole mock-up is simulated, therefore the components (or domains

according to the COMSOL nomenclature) inserted in the models resemble the different layers that compose the mock-up. All the domains, even the air channel, are simulated as rectangles, having a height of 1 m and a characteristic thickness in line with the components' real dimensions. The LSC panel and the Al pane are, respectively, 0.5 cm and 0.3 cm thick and a 9 cm domain is inserted between them to simulate the narrow air cavity. To model the insulating material next to the Al absorber, a 5.5 cm-thick domain is inserted, which is followed by a 12 cm-thick rectangle representing the mock-up brick layer.

This domain structure is the one implemented in the calibration model and represents the CFM, whereas, in the OFM, two supplementary fluid domains are implemented. The first one is placed under the VF air cavity and is simulated as a rectangle having a channel width of 9 cm and a height of 0.13 m, whereas the second is added to the top of the channel. It is simulated having the same width and a height of 0.5 m. Their addition is discretionary; the top add-on is implemented for a better modeling of air flow in proximity of the channel outlet, whereas the bottom domain is inserted to consider the impact of a peculiar condition that influences the experimental data. The mock-up, in fact, is installed on a reflective floor with the channel inlet close to it, thus the temperature and the flow of air entering the cavity is partially modified by the reflected solar radiation. The bottom domain is simulated at 0.13 m high, as it corresponds to the mock-up height with respect to the reflective floor. The domains inserted in the OFM and CFM are presented in Table 1.

Table 1. Description of the geometry implemented in the different models.

Model Typology	FEM Model	Domain	Dimensions (t × h)	COMSOL Layout
Calibration Model	Closed Façade Model	LSC	0.5 cm × 100 cm	
		Air Cavity	9 cm × 100 cm	
		Back Panel	0.3 cm × 100 cm	
		Insulating Layer	5.5 cm × 100 cm	
		Hollow Bricks	12 cm × 100 cm	
Validation Model	Open Façade Model	LSC	0.5 cm × 100 cm	
		Air Cavity	9 cm × 100 cm	
		Back Panel	0.3 cm × 100 cm	
		Insulating Layer	5.5 cm × 100 cm	
		Hollow Bricks	12 cm × 100 cm	
		Top Add-on ¹	9 cm × 50 cm	
Bottom Add-on ¹	9 cm × 13 cm			

¹ Domains functional to the air-flow modeling.

2.3.1. Boundary Conditions

In both the CFM and OFM, the temperature measured by the NTC of Level 1 is imposed as a temperature constraint along the inner boundary of the wall domain. Additionally, in these models, the conditions applied to the external boundary of the LSC domain are kept unchanged, since they consist of the measured GNI and the convective heat flux of Expression (9).

To model the nonideality of the thermal coupling between the Al panel and the XPS, a contact resistive layer having an equivalent thermal resistance of $R_{EQ} = 2 \text{ (K} \cdot \text{m}^2) / \text{W}$ is implemented between the two layers. The choice of this value is based on the employed materials and the operating conditions, as well as the literature evidence [66,67]. Regarding the SPF boundary conditions, in both the CFM and OFM, the vertical edges of the channel walls are assigned the no-slip condition, while the buoyancy phenomenon is implemented by modeling air as a weakly compressible fluid and by introducing the gravity force.

In the CFM, the same SPF boundary conditions are also imposed on the horizontal edges of the channel; they are considered as thermally insulated in the HT physics accordingly with the experimental set-up. Finally, to ensure the model convergence, a pressure point constraint having a value equal to the atmospheric one is inserted at the bottom of the channel.

As mentioned in Section 2.3. (*Model Domains*), two additional domains are added for the OFM. Air exiting the upper one is modeled by defining its top edge as an outlet having variable temperature and atmospheric pressure. Air entering the lower fluid domain is simulated by setting its bottom edge as the inflow, having a pressure equal to the ambient pressure but a temperature two degrees higher with respect to the ambient temperature. This measure is adopted since the proximity of the channel inlet to the roof covering increases the temperature of the air entering the channel. Tables S1 and S2 summarize the boundary conditions inserted in the different physics of the developed models, as well as the related COMSOL layout.

2.3.2. Model Meshing

To minimize both the numerical errors and the computational time, the developed models are meshed by combining two bidimensional mapping structures. In particular, the air cavity is meshed by using unstructured triangular elements, whereas the remaining domains are meshed by creating structured quadrilateral elements representing a swipe of the mesh generated inside the cavity. To ensure a correct modeling of the air-buoyancy phenomenon, the elements' density within the ventilation channel and in the near areas is increased. Moreover, the quality of the mesh is further improved by the implementation of two general features: one decreases the element size at sharp corners (Corner Refinement) and the other typically uses in-fluid flow problems with no-slip boundary conditions (Boundary Layers). They are introduced to resolve the thin boundary layers that are created along cavity edges, as this feature generates a denser element distribution in the direction normal to the flow. The whole mesh is composed of triangular linear elements with 42,525 degrees of freedom for the CFM and 53,338 for the OFM. To improve the solution, a finer mesh is implemented inside the ventilation channel and in the adjacent areas.

2.4. Optical Measurements

Given the wide range of wavelengths necessary to properly model the system radiative property, the optical parameters of the VF are modeled thanks to a combination of experimental measurements and the literature evidence. In particular, the LSC and aluminum optical properties in the 350 nm–800 nm range are directly measured, thus ensuring a higher correspondence between the real and the simulated spectra, especially for the one transmitted by the LSC panel.

To guarantee a continuous emission in the range of interest, the optical measurements are performed by using a UV-VIS-NIR light source (Ocean Insight DH-2000-S-DUV-TTL) equipped with a deuterium arc lamp and tungsten–halogen light bulb. To estimate the reflectance, σ , of both the LSC and the Al pane, the output of the light source is coupled with an Integrating Sphere (IS) specifically designed for these measurements, by using a quartz optic fibre. A second quartz optic fibre is used to connect the IS to an Ocean Optics USB4000-XR1-ES spectrometer with an UV-VIS-NIR sampling range, thus collecting the light reflected by the samples. Since the LSC slab is a semi-transparent object, its transmittance is also acquired by a procedure similar to the one described in the Supplementary Materials of Ref. [38]. The only difference is the positioning of the IS; to ensure the collection of the fluorescent light, it is placed next to the sample. The emissivity ε of the different surfaces is then obtained, thanks to Equation (11):

$$\varepsilon + \tau + \sigma = 1 \quad (11)$$

where for the Al pane, the transmittance τ is set equal to zero. The measured values and the functions implemented in COMSOL as materials' optical properties are reported in Figure 4.

2.5. Uncertainties Estimation

The uncertainties affecting the experimental data are determined thanks to the accuracy of the measuring instruments for the directly measured physical quantities or by using Equation (12) for the indirect ones [68].

$$u_i^2 = \sum_{i=1}^n \left(\frac{\partial f}{\partial x_i} \right)^2 u_d^2(x_i), \quad (12)$$

where u_i is the estimated error on the indirect measurement, $f(x_1, x_2, \dots, x_n)$ is the indirect physical quantity function of the direct parameters x_i , and u_d is its uncertainty.

Being indirectly measured by the NTC resistance variation, the uncertainty on the measured temperatures is evaluated thanks to Equation (12). The absolute error ranges from 0.3 °C to 0.5 °C and is obtained by propagating the 1% accuracy declared for both the measured resistance value and the NTC characteristic coefficient (see Equation (S1)). Considering the variability of the uncontrolled environment in which the experimental data are acquired, the uncertainty used within this work is 0.5 °C. The uncertainties of the used sensors are summarised in Table 2.

Table 2. Uncertainties of the temperature, wind, and irradiance sensors.

Measured Physical Quantity	Uncertainty
Temperature	±0.5 °C
Wind velocity	±0.5 m/s
Irradiance	±20 W/m ²

The discrepancy between the measured and simulated data are defined thanks to the statistical estimators reported in [69], namely the Root Mean Square Error (RMSE), the Coefficient of Variation of the Root Mean Square Error (CVRMSE), and the Normalized Mean Biased Error (NMBE). The indices are defined as follows:

$$RMSE = \sqrt{\frac{\sum_{i=1}^N (y_i - \hat{y}_i)^2}{N}}, \quad (13)$$

$$NMBE = \frac{1}{y_m} \left(\frac{\sum_{i=1}^N (y_i - \hat{y}_i)}{N} \right) \cdot 100, \quad (14)$$

$$CVRMSE = \frac{1}{y_m} \sqrt{\frac{\sum_{i=1}^N (y_i - \hat{y}_i)^2}{N}} \cdot 100, \quad (15)$$

where \hat{y}_i are the simulated data, y_i are the measured data, y_m is the mean of the measured data, and N is the population numerosness.

According to Wijesuriya et al. [69], a CVRMSE between ±15% and a NMBE between ±5% can be considered as high standard calibration criteria.

3. Results and Discussion

Pasut and De Clari investigated the relevant elements in the simulation of a naturally VF using a CFD mode and concluded that, considering the nature of velocity field inside the air cavity, this type of system can be simulated with 2D models [65]. The presence of three different sensor submatrixes crossing all the mock-up layers ensured the verification of this hypothesis. In Table 3, the comparison between the temperatures measured by the Left (L), Central (C), and Right (R) sections of Level 4 and Level 5 are reported. The analyzed values refer to two data acquisition campaigns; the first measurements occurred from 13 to 18 June 2021 in the closed façade configuration, whereas the second occurred between 9 and 14 September 2021, with the cavity naturally ventilated.

Table 3. Temperatures of LSC and back panel measured at different hours in different façade configurations.

Configuration	Daytime	GNI (W/m ²)	v _{wind} (m/s)	T _{LSC} (°C)			T _{AI} (°C)		
				L	C	R	L	C	R
Closed Channel ¹	00:00	0	1.29	21.6	21.0	21.8	25.4	24.1	25.3
	06:00	94	3.84	24.7	24.9	24.6	25.4	25.5	25.5
	12:00	553	1.27	47.5	47.1	47.7	51.1	51.1	51.1
	18:00	32	1.36	24.8	25.2	25.4	30.2	30.1	30.3
Naturally Ventilated Channel ²	00:00	0	0.79	17.3	17.4	17.1	20.3	20.2	20.3
	06:00	60	0.24	15.0	15.8	16.2	17.3	17.1	17.2
	12:00	767	0.75	51.0	51.7	51.1	46.7	46.9	46.1
	18:00	1	1.90	23.4	23.3	23.3	26.1	25.7	25.5

¹ The compared data were acquired 15 June 2021; ² the compared data were acquired 11 September 2021.

The results presented in Table 3 corroborate the hypothesis of a 2D modeling for the estimation of the VF performance. However, the exposure of the mock-up to an uncontrolled environment required a careful assessment of the data used in the model calibration and validation.

The effect of the environmental parameters on the temperature measured by the NTC was estimated by evaluating the impact of the wind velocity on the acquired data and is presented in Figure S5.

Considering the non-negligible influence of the ambient conditions on the measured temperatures, as the data source for the calibration and validation of the models, the temperatures measured by the NTC of the third row of the central section were selected. In fact, it was reasonable to suppose that these sensors were the least affected by the abrupt changes in the uncontrolled environment conditions.

3.1. Model Validation

The physical properties inserted in the CFM and OFM were calibrated and validated against the data acquired in both open and closed façade configurations. The thermal properties attributed to each domain are reported in Table 4 and the optical properties are presented in Table 5.

Table 4. Thermal properties inserted in the HT and SPF physics for the developed models.

Mock-Up Component	Physical Parameter		
	λ (W/(m·K))	ρ (kg/m ³)	C _p (J/(kg·K))
LSC	0.19	1180	1466
Back Panel	237	2700	900
XPS	0.037	1300	80
Hollow Bricks	0.24	840	500

Table 5. Optical properties attributed to the LSC and the AI back panel in the RAD physics for CFM and OFM.

λ_{start} (μm)	λ_{end} (μm)	ϵ_{LSC}	ϵ_{AI}	ϵ_{amb}	LSC _{Opacity}	AI _{Opacity}
0	0.38	0.90	0.06	1	OP	OP
0.38	0.42	0.75	0.06	1	OP	OP
0.42	0.46	0.93	0.06	1	OP	OP
0.46	0.5	0.83	0.06	1	OP	OP
0.5	0.61	0.95	0.06	1	OP	OP
0.61	2.5	0.05	0.07	1	TR	OP
2.5	8	0.05	0.05	1	TR	OP
8	13	0.05	0.01	0.3	TR	OP
13	25	0.05	0.01	0.9	TR	OP

The thermal properties attributed to the modeled materials are within the literature ranges, apart for the XPS ones. Indeed, they were obtained by considering that the insulation layer was formed by a combination of an XPS panel with polyurethane foam added to ensure the adhesion between the bricks and the XPS panel. The thermal properties of the air inserted in the domains defined as fluid are not reported as they were COMSOL default functions taken by the embedded material library.

The LSC and AI optical properties were simulated thanks to piecewise functions having an interval delimited by the values termed as λ_{start} and λ_{end} .

The emissivity ϵ_{LSC} was attributed to both the internal and external LSC surfaces, whereas ϵ_{AI} was attributed only to the back panel edge facing the LSC.

3.2. Data Comparison

The simulated temperatures obtained under these hypotheses are presented in Figure 5, in which they are graphically compared with the measured ones. Figure 5a displays the results relative to the CFM obtained during the data acquisition campaign of June, whose measurements were used as the calibration set. Figure 5b presents the naturally ventilated configuration dataset relative to the measurements taken during the acquisition campaign of September, which were used as the validation set.

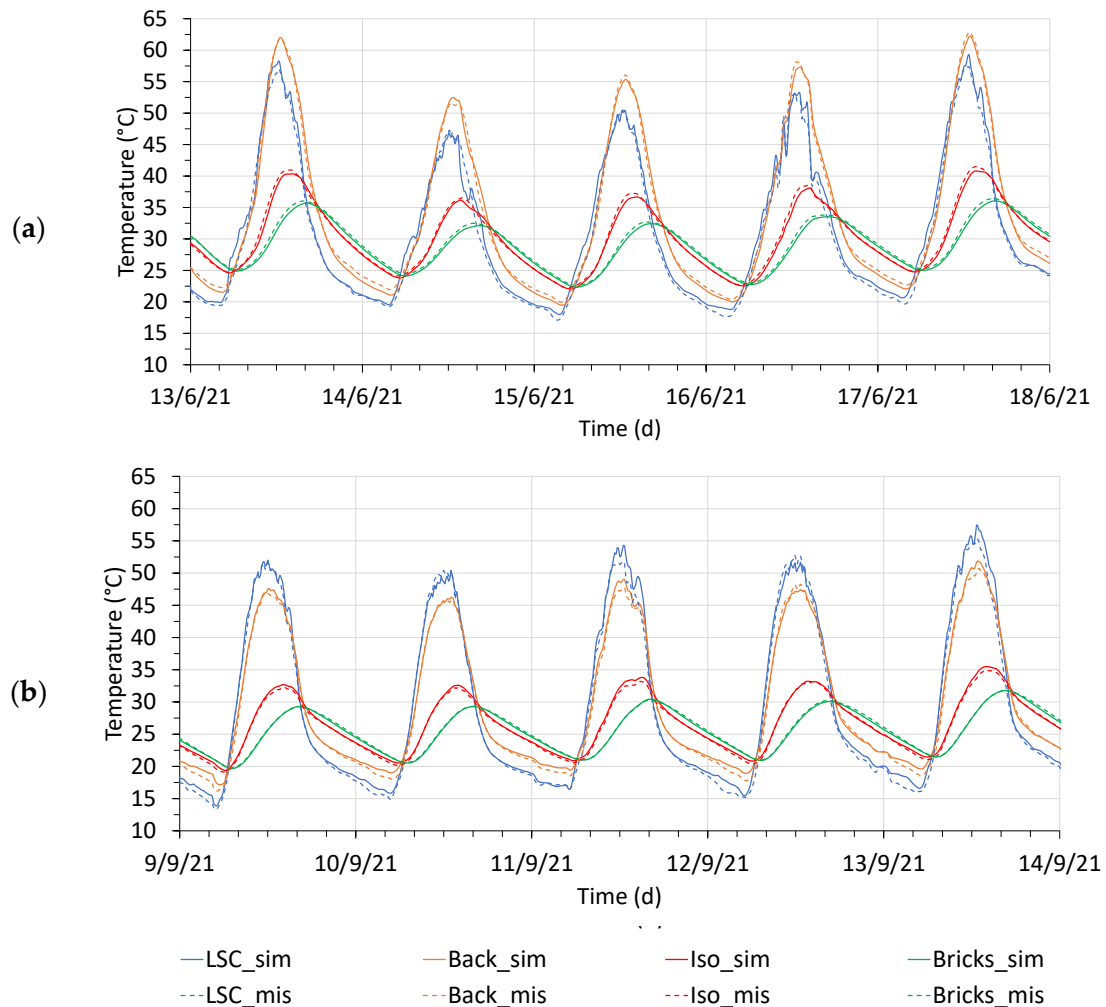


Figure 5. Comparison between measured (dashed lines) and simulated (continuous lines) temperature of the façade layers in the (a) CFM and (b) OFM.

The simulated results were obtained after the verification of the model mesh independency, which is presented in Figure 6.

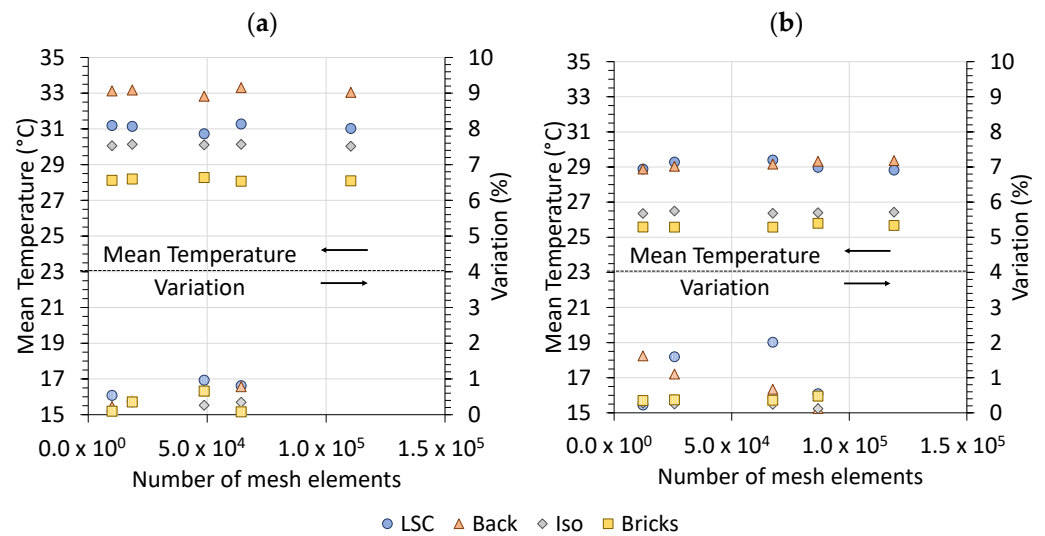


Figure 6. Mesh independence study (a) CFM, (b) OFM.

As the quantitative estimator of the mesh quality, a parameter called skewness is used. Having a value ranging between 0 and 1, it evaluates the distortion of each mesh element with respect to the ideal one. Differently from the usual convention, COMSOL associates a skewness equal to 1 to ideal elements and 0 to highly distorted ones. Both the meshes employed for the CFM and the OFM present an average skewness of 0.95.

According to Section 2.5. (*Uncertainties Estimation*), the discrepancy between the measured and the simulated temperature are estimated through the RMSE, the NMBE, and the CV (RMSE), whose values are reported in Table 6.

Table 6. NMBE and CVRMSE of the CFM and OFM.

Estimator	Closed Façade Configuration				Open Façade Configuration			
	LSC	Back	XPS	Bricks	LSC	Back	XPS	Bricks
RMSE	1.4 °C	0.8 °C	0.5 °C	0.4 °C	1.2 °C	0.7 °C	0.3 °C	0.2 °C
NMBE	−2.9%	0.9%	0.6%	1.2%	−2.5%	−1.5%	−0.9%	0.5%
CV(RMSE)	4.9%	2.8%	1.9%	1.7%	4.1%	2.3%	1.3%	0.7%

Considering that the experimental data were acquired by exposing the mock-up to unrestrained environmental conditions, the obtained RMSEs are in accordance with the literature [70].

3.3. LSC Panel Electrical Performance

The results concerning the LSC panel electrical performance are presented in Figure S4, highlighting a maximum peak power of 2.25 W under a GNI of 480 W/m² and an electrical efficiency of 0.5%. Considering the slab dimensions and the employed PV cells, the latter value is perfectly aligned with those found in the literature [41–43].

4. Conclusions

The research proposed here is a preliminary numerical and experimental investigation aimed at evaluating the coupling of two deeply studied topics, namely LSC panels and VFs. On the one hand, LSC panels have gained attention for their high transparency and low number of photovoltaic cells for the active area, which makes them an appealing architectural application. On the other hand, VFs have proved their efficacy as a passive cooling technique by reducing the solar gain through the building envelope during the summer, hence reducing the energy required for cooling. Even though much research

has focused on each of these concepts, individually their combination (which might bring further improvements) has not yet been deeply studied. An attempt to bridge this gap of knowledge was made by realizing the experimental mock-up of a VF module that was clad with a LSC panel. The interaction between the different system components, as well as their physical properties, was estimated by the comparison between the experimental data and the simulated results, for which the usage of a multi-physical software such as COMSOL has proven to be essential. The models simulating closed and natural ventilated façade configurations were calibrated and validated against separated data acquisition campaigns, showing a good agreement between the experimental and the numerical values, with a minimum RMSE of 0.4 °C for the layer less subjected to a variation of the ambient conditions and a maximum one of 1.4 °C for the layer most affected by the environmental parameters. Moreover, the monitoring of the LSC panel performance proved that this module can be effectively integrated in the building envelope, reporting a power conversion efficiency value equal to 0.5%. The results obtained here encourage further investigations aimed at evaluating the thermal performance of the proposed system applied on a realistic building, to be conducted by means of dynamic simulation software, through which any energy savings could be assessed. Further explorations might also focus on different internal skin typologies in order to maximize the achievable effects.

Supplementary Materials: The following supporting information can be downloaded at: <https://www.mdpi.com/article/10.3390/su15129146/s1>, Figure S1: Block diagram presenting the components and the logical connection of the data acquisition system; Figure S2: Schematic of the voltage divider used to constrain the voltage drop on the NTC between 0 and 2.048 V corresponding to temperatures ranging from $+\infty$ to -8.6 °C. The purpose of the pull-down resistor is to avoid the voltage swing limit of the input amplifier; Figure S3: Measurable temperature range by the NTC sensors as a function of the potential difference between $V+$ and $V-$; Figure S4: (a) LSC panel I-V and P-V curves measured under a GNI of 480 W/m² (4 May 2021). (b) Efficiency and power produced by the module between the 4 and 9 May 2021. Figure S5: (a) Range of possible convective heat flux according to the anemometer accuracy. Simulated (b) LSC, and (c) Al pane temperature ranges according to the different h used in the CFM; Table S1: Summary of the boundary conditions inserted in the CFM; Table S2: Summary of the new boundary conditions inserted in the OFM.

Author Contributions: Conceptualization, G.M. and D.V.; methodology, G.M. and E.B.; software, G.M. and P.B.; validation, G.M.; formal analysis, G.M. and E.B.; investigation, G.M.; resources, D.V.; data curation, G.M. and V.D.; writing—original draft preparation, G.M.; writing—review and editing, A.A. and V.D.; visualization, G.M.; supervision, P.B.; project administration, D.V.; funding acquisition, D.V. All authors have read and agreed to the published version of the manuscript.

Funding: This work was developed within a project entitled Development of photovoltaic ventilated facade-smart skin- for the control of buildings thermal budget, which was part of the POR FESR 2014–2020 program funded by Regione Emilia Romagna and European Union.

Institutional Review Board Statement: Not applicable.

Informed Consent Statement: Not applicable.

Data Availability Statement: Data are contained within the article and the correlated Supplementary Materials.

Acknowledgments: Thanks to Michele Bottarelli, at the Department of Architecture of the Ferrara University, for his precious advice regarding the development of numerical simulations by using COMSOL Multiphysics, without which this contribution would not have been possible.

Conflicts of Interest: The authors declare no conflict of interest.

References

1. Xiang, X.; Ma, M.; Ma, X.; Chen, L.; Cai, W.; Feng, W.; Ma, Z. Historical Decarbonization of Global Commercial Building Operations in the 21st Century. *Appl. Energy* **2022**, *322*, 119401. [[CrossRef](#)]
2. Ma, M.; Feng, W.; Huo, J.; Xiang, X. Operational Carbon Transition in the Megalopolises' Commercial Buildings. *Build. Environ.* **2022**, *226*, 109705. [[CrossRef](#)]

3. Aldegheri, F.; Baricordi, S.; Bernardoni, P.; Brocato, M.; Calabrese, G.; Guidi, V.; Mondardini, L.; Pozzetti, L.; Tonezzer, M.; Vincenzi, D. Building Integrated Low Concentration Solar System for a Self-Sustainable Mediterranean Villa: The Astonysine House. *Energy Build.* **2014**, *77*, 355–363. [[CrossRef](#)]
4. Zarcone, R.; Brocato, M.; Bernardoni, P.; Vincenzi, D. Building Integrated Photovoltaic System for a Solar Infrastructure: Liv-Lib' Project. *Energy Procedia* **2016**, *91*, 887–896. [[CrossRef](#)]
5. Vincenzi, D.; Aldegheri, F.; Baricordi, S.; Bernardoni, P.; Calabrese, G.; Guidi, V.; Pozzetti, L. Low Concentration Solar Louvres for Building Integration. *AIP Conf. Proc.* **2013**, *1556*, 110–113.
6. Maghrabie, H.M.; Elsaid, K.; Sayed, E.T.; Abdelkareem, M.A.; Wilberforce, T.; Olabi, A.G. Building-Integrated Photovoltaic/Thermal (BIPVT) Systems: Applications and Challenges. *Sustain. Energy Technol. Assess.* **2021**, *45*, 101151. [[CrossRef](#)]
7. Boschetti, M.; Vincenzi, D.; Mangherini, G.; Bernardoni, P.; Andreoli, A.; Gjestila, M.; Camattari, R.; Fugattini, S.; Caramori, S.; Cristino, V.; et al. Modular Stand-Alone Photoelectrocatalytic Reactor for Emergent Contaminant Degradation via Solar Radiation. *Sol. Energy* **2021**, *228*, 120–127. [[CrossRef](#)]
8. Mukhopadhyay, B.; Das, D. Multi-Objective Dynamic and Static Reconfiguration with Optimized Allocation of PV-DG and Battery Energy Storage System. *Renew. Sustain. Energy Rev.* **2020**, *124*, 109777. [[CrossRef](#)]
9. Diolaiti, V.; Andreoli, A.; Bernardoni, P.; Mangherini, G.; Ouelhazi, M.A.; Venezia, E.; Ricci, M.; Proietti, R.Z.; Vincenzi, D. Nanostructured Germanium Anode for Lithium-Ion Batteries for Aerospace Technologies. In Proceedings of the 2022 IEEE 22nd International Conference on Nanotechnology (NANO), Palma de Mallorca, Spain, 4–8 July 2022; pp. 56–59.
10. Fugattini, S.; Gulzar, U.; Andreoli, A.; Carbone, L.; Boschetti, M.; Bernardoni, P.; Gjestila, M.; Mangherini, G.; Camattari, R.; Li, T.; et al. Binder-Free Nanostructured Germanium Anode for High Resilience Lithium-Ion Battery. *Electrochim. Acta* **2022**, *411*, 139832. [[CrossRef](#)]
11. Athienitis, A.K.; Barone, G.; Buonomano, A.; Palombo, A. Assessing Active and Passive Effects of Façade Building Integrated Photovoltaics/Thermal Systems: Dynamic Modelling and Simulation. *Appl. Energy* **2018**, *209*, 355–382. [[CrossRef](#)]
12. Ortiz Lizcano, J.C.; Haghighi, Z.; Wapperom, S.; Infante Ferreira, C.; Isabella, O.; vd Dobbelsteen, A.; Zeman, M. Photovoltaic Chimney: Thermal Modeling and Concept Demonstration for Integration in Buildings. *Prog. Photovolt. Res. Appl.* **2020**, *28*, 465–482. [[CrossRef](#)]
13. Corrao, R.; La Placa, E. Plaster Ventilated Fa Ade System for Renovating Modern and Ancient Buildings. A CFD Analysis. *IOP Conf. Ser. Earth Environ. Sci.* **2021**, *863*, 012046. [[CrossRef](#)]
14. De Boeck, L.; Verbeke, S.; Audenaert, A.; De Mesmaeker, L. Improving the Energy Performance of Residential Buildings: A Literature Review. *Renew. Sustain. Energy Rev.* **2015**, *52*, 960–975. [[CrossRef](#)]
15. Onbasioglu, H.; Egrican, A.N. Experimental Approach to the Thermal Response of Passive Systems. *Energy Convers. Manag.* **2002**, *43*, 2053–2065. [[CrossRef](#)]
16. Shameri, M.A.; Alghoul, M.A.; Sopian, K.; Zain, M.F.M.; Elayeb, O. Perspectives of Double Skin Façade Systems in Buildings and Energy Saving. *Renew. Sustain. Energy Rev.* **2011**, *15*, 1468–1475. [[CrossRef](#)]
17. Pomponi, F.; Piroozfar, P.A.E.; Southall, R.; Ashton, P.; Farr, E.R.P. Energy Performance of Double-Skin Façades in Temperate Climates: A Systematic Review and Meta-Analysis. *Renew. Sustain. Energy Rev.* **2016**, *54*, 1525–1536. [[CrossRef](#)]
18. Pappas, A.; Zhai, Z. Numerical Investigation on Thermal Performance and Correlations of Double Skin Façade with Buoyancy-Driven Airflow. *Energy Build.* **2008**, *40*, 466–475. [[CrossRef](#)]
19. Parhizkar, H.; Khoraskani, R.A.; Tahbaz, M. Double Skin Façade with Azolla; Ventilation, Indoor Air Quality and Thermal Performance Assessment. *J. Clean. Prod.* **2020**, *249*, 119313. [[CrossRef](#)]
20. Biyik, E.; Araz, M.; Hepbasli, A.; Shahrestani, M.; Yao, R.; Shao, L.; Essah, E.; Oliveira, A.C.; del Caño, T.; Rico, E.; et al. A Key Review of Building Integrated Photovoltaic (BIPV) Systems. *Eng. Sci. Technol. Int. J.* **2017**, *20*, 833–858. [[CrossRef](#)]
21. Pérez-Grande, I.; Meseguer, J.; Alonso, G. Influence of Glass Properties on the Performance of Double-Glazed Facades. *Appl. Therm. Eng.* **2005**, *25*, 3163–3175. [[CrossRef](#)]
22. Chan, A.L.S.; Chow, T.T.; Fong, K.F.; Lin, Z. Investigation on Energy Performance of Double Skin Façade in Hong Kong. *Energy Build.* **2009**, *41*, 1135–1142. [[CrossRef](#)]
23. Gregório-Atem, C.; Aparicio-Fernández, C.; Coch, H.; Vivancos, J.L. Opaque Ventilated Façade (OVF) Thermal Performance Simulation for Office Buildings in Brazil. *Sustainability* **2020**, *12*, 7635. [[CrossRef](#)]
24. Gonçalves, J.E.; van Hooff, T.; Saelens, D. Simulating Building Integrated Photovoltaic Facades: Comparison to Experimental Data and Evaluation of Modelling Complexity. *Appl. Energy* **2021**, *281*, 116032. [[CrossRef](#)]
25. Gratia, E.; De Herde, A. Natural Ventilation in a Double-Skin Façade. *Energy Build.* **2004**, *36*, 137–146. [[CrossRef](#)]
26. Rahmani, B.; Kandar, M.Z.; Rahmani, P. How Double Skin Façade's Air-Gap Sizes Effect on Lowering Solar Heat Gain in Tropical Climate? *World Appl. Sci. J.* **2012**, *18*, 774–778. [[CrossRef](#)]
27. Quesada, G.; Rousse, D.; Dutil, Y.; Badache, M.; Hallé, S. A Comprehensive Review of Solar Facades. Opaque Solar Facades. *Renew. Sustain. Energy Rev.* **2012**, *16*, 2820–2832. [[CrossRef](#)]
28. Quesada, G.; Rousse, D.; Dutil, Y.; Badache, M.; Hallé, S. A Comprehensive Review of Solar Facades. Transparent and Translucent Solar Facades. *Renew. Sustain. Energy Rev.* **2012**, *16*, 2643–2651. [[CrossRef](#)]
29. Visa, I.; Comsit, M.; Duta, A. Urban Acceptance of Façade Integrated Novel Solar Thermal Collectors. *Energy Procedia* **2014**, *48*, 1429–1435. [[CrossRef](#)]

30. Escarre, J.; Li, H.Y.; Sansonnens, L.; Galliano, F.; Cattaneo, G.; Heinsteinst, P.; Nicolay, S.; Bailat, J.; Eberhard, S.; Ballif, C.; et al. When PV Modules Are Becoming Real Building Elements: White Solar Module, a Revolution for BIPV. In Proceedings of the 2015 IEEE 42nd Photovoltaic Specialist Conference (PVSC), New Orleans, LA, USA, 14–19 June 2015; pp. 1–2. [CrossRef]
31. Morlier, A.; Lim, B.; Blankemeyer, S.; Schulte-huxel, H.; Witteck, R.; Daschinger, T.; Bräunig, S.; Köntges, M.; Brendel, R. Photovoltaic Modules with the Look and Feel of a Stone Façade for Building Integration. *Solar RRL* **2021**, *6*, 2100356. [CrossRef]
32. Yu, H.; Wang, Q.; Lu, C.; Wei, C. The Research on a New Type of BIPV Modules Constructed by Thin-Film Photovoltaic Panel (or Module)/PU/Color Organic-Coated Steel Plate. In Proceedings of the 2015 IEEE 42nd Photovoltaic Specialist Conference (PVSC), New Orleans, LA, USA, 14–19 June 2015; pp. 2724–2727. [CrossRef]
33. Dhere, N.G.; Shiradkar, N.; Schneller, E.; Gade, V. The Reliability of Bypass Diodes in PV Modules. *Reliab. Photovolt. Cells Modul. Compon. Syst. VI* **2013**, 8825, 88250I. [CrossRef]
34. Pagliaro, M.; Ciriminna, R.; Palmisano, G. BIPV: Merging the Photovoltaic with the Construction Industry. *Prog. Photovolt. Res. Appl.* **2010**, *18*, 61–72. [CrossRef]
35. Maggioni, G.; Campagnaro, A.; Carturan, S.; Quaranta, A. Dye-Doped Parylene-Based Thin Film Materials: Application to Luminescent Solar Concentrators. *Sol. Energy Mater. Sol. Cells* **2013**, *108*, 27–37. [CrossRef]
36. Correia, S.F.H.; De Zea Bermudez, V.; Ribeiro, S.J.L.; André, P.S.; Ferreira, R.A.S.; Carlos, L.D. Luminescent Solar Concentrators: Challenges for Lanthanide-Based Organic-Inorganic Hybrid Materials. *J. Mater. Chem. A* **2014**, *2*, 5580–5596. [CrossRef]
37. Bomm, J.; Büchtemann, A.; Chatten, A.J.; Bose, R.; Farrell, D.J.; Chan, N.L.A.; Xiao, Y.; Slooff, L.H.; Meyer, T.; Meyer, A.; et al. Fabrication and Full Characterization of State-of-the-Art Quantum Dot Luminescent Solar Concentrators. *Sol. Energy Mater. Sol. Cells* **2011**, *95*, 2087–2094. [CrossRef]
38. Bernardoni, P.; Mangherini, G.; Gjestila, M.; Andreoli, A.; Vincenzi, D. Performance Optimization of Luminescent Solar Concentrators under Several Shading Conditions. *Energies* **2021**, *14*, 816. [CrossRef]
39. SunPower. *Technical Data Sheet: C50 Solar Cell Mono Crystalline Silicon*; SunPower Inc.: San Jose, CA, USA, 2010.
40. Tonezzer, M.; Gutierrez, D.; Vincenzi, D. Luminescent Solar Concentrators—State of the Art and Future Perspectives. In *Solar Cell Nanotechnology*; Wiley Online Library: Hoboken, NJ, USA, 2013; pp. 293–315. ISBN 9781118845721.
41. Rafiee, M.; Chandra, S.; Ahmed, H.; McCormack, S.J. An Overview of Various Configurations of Luminescent Solar Concentrators for Photovoltaic Applications. *Opt. Mater.* **2019**, *91*, 212–227. [CrossRef]
42. Bognár, Á.; Kusnadi, S.; Slooff, L.H.; Tzikas, C.; Loonen, R.C.G.M.; de Jong, M.M.; Hensen, J.L.M.; Debije, M.G. The Solar Noise Barrier Project 4: Modeling of Full-Scale Luminescent Solar Concentrator Noise Barrier Panels. *Renew. Energy* **2020**, *151*, 1141–1149. [CrossRef]
43. Aste, N.; Buzzetti, M.; Del Pero, C.; Fusco, R.; Leonforte, F.; Testa, D. Triggering a Large Scale Luminescent Solar Concentrators Market: The Smart Window Project. *J. Clean. Prod.* **2019**, *219*, 35–45. [CrossRef]
44. COMSOL. *Multiphysics Reference Manual*; COMSOL Inc.: Stockholm, Sweden, 2021.
45. De Gracia, A.; Castell, A.; Navarro, L.; Oró, E.; Cabeza, L.F. Numerical Modelling of Ventilated Facades: A Review. *Renew. Sustain. Energy Rev.* **2013**, *22*, 539–549. [CrossRef]
46. DELO Industrial Adhesives. *Technical Data Sheet: DELO-PHOTOBOND GB368*; DELO Industrial Adhesives: Windach, Germany, 2014.
47. 3M. *Technical Data Sheet: DF2000MA Release B*; 3M: St. Paul, MN, USA, 2015.
48. Schlegel, F. COMSOL: Using the Boussinesq Approximation for Natural Convection. Available online: <https://www.comsol.com/blogs/using-the-boussinesq-approximation-for-natural-convection/> (accessed on 13 January 2022).
49. Porotherm Technical Datasheet Porotherm. BIO Inc. 12. Available online: https://www.wienerberger.it/content/dam/wienerberger/italy/marketing/documents-magazines/technical/technical-product-info-sheet/wall/Sch_tec_Pth_BIO_inc_12x50x19_BUB.pdf (accessed on 15 February 2022).
50. MIT. PMMA Properties. Available online: <http://www.mit.edu/~6.777/matprops/pmma.htm> (accessed on 3 May 2022).
51. Li, Q.; Wu, A.-p.; Li, Y.-j.; Wang, G.-q.; Qi, B.-j.; Yan, D.-y.; Xiong, L.-y. Segregation in Fusion Weld of 2219 Aluminum Alloy and Its Influence on Mechanical Properties of Weld. *Trans. Nonferrous Met. Soc. China (Engl. Ed.)* **2017**, *27*, 258–271. [CrossRef]
52. Brandt, R.; Neuer, G. Electrical Resistivity and Thermal Conductivity of Pure Aluminum and Aluminum Alloys up to and above the Melting Temperature. *Int. J. Thermophys.* **2007**, *28*, 1429–1446. [CrossRef]
53. Borgohain, C.; Acharyya, K.; Sarma, S.; Senapati, K.K.; Sarma, K.C.; Phukan, P. A New Aluminum-Based Metal Matrix Composite Reinforced with Cobalt Ferrite Magnetic Nanoparticle. *J. Mater. Sci.* **2013**, *48*, 162–171. [CrossRef]
54. IUAV. *Materiali Isolanti Nuove Tendenze in Architettura*. Available online: https://www.iuav.it/SISTEMA-DE/Archivio-d/approfondi/materiali-/Materiali_Isolanti.pdf (accessed on 17 February 2022).
55. COMSOL. Greenhouse Effect. Available online: <https://www.comsol.it/model/greenhouse-effect-98061> (accessed on 2 January 2022).
56. Rashidian, M.; Dorrnanian, D. Low-Intensity UV Effects on Optical Constants of PMMA Film. *J. Theor. Appl. Phys.* **2014**, *8*, 121. [CrossRef]
57. Ayieko, C.O.; Musembi, R.J.; Ogacho, A.A.; Aduda, B.O.; Muthoka, B.M.; Jain, P.K. Controlled Texturing of Aluminum Sheet for Solar Energy Applications. *Adv. Mater. Phys. Chem.* **2015**, *05*, 458–466. [CrossRef]
58. Ahmed, R.M. Optical Study on Poly(Methyl Methacrylate)/Poly(Vinyl Acetate) Blends. *Int. J. Photoenergy* **2009**, *2009*, 150389. [CrossRef]

59. Wen, C.-D.; Mudawar, I. Emissivity Characteristics of Polished Aluminum Alloy Surfaces and Assessment of Multispectral Radiation Thermometry (MRT) Emissivity Models. *Int. J. Heat Mass Transf.* **2005**, *48*, 1316–1329. [[CrossRef](#)]
60. Estalote, E.A.; Ramanathan, K.G. Low-Temperature Emissivities of Copper and Aluminum. *J. Opt. Soc. Am.* **1977**, *67*, 39. [[CrossRef](#)]
61. Evangelisti, L.; Guattari, C.; Asdrubali, F. On the Sky Temperature Models and Their Influence on Buildings Energy Performance: A Critical Review. *Energy Build.* **2019**, *183*, 607–625. [[CrossRef](#)]
62. Albatayneh, A.; Alterman, D.; Page, A.; Moghtaderi, B. The Significance of Sky Temperature in the Assessment of the Thermal Performance of Buildings. *Appl. Sci.* **2020**, *10*, 8057. [[CrossRef](#)]
63. COMSOL. Radiative Cooling. Available online: <https://www.comsol.it/model/radiative-cooling-75021> (accessed on 22 December 2021).
64. Ong, K.S. A Mathematical Model of a Solar Chimney. *Renew. Energy* **2003**, *28*, 1047–1060. [[CrossRef](#)]
65. Pasut, W.; De Carli, M. Evaluation of Various CFD Modelling Strategies in Predicting Airflow and Temperature in a Naturally Ventilated Double Skin Faade. *Appl. Therm. Eng.* **2012**, *37*, 267–274. [[CrossRef](#)]
66. Fiedler, T.; White, N.; Dahari, M.; Hooman, K. On the Electrical and Thermal Contact Resistance of Metal Foam. *Int. J. Heat Mass Transf.* **2014**, *72*, 565–571. [[CrossRef](#)]
67. Casalegno, V.; Vavassori, P.; Valle, M.; Ferraris, M.; Salvo, M.; Pintsuk, G. Measurement of Thermal Properties of a Ceramic/Metal Joint by Laser Flash Method. *J. Nucl. Mater.* **2010**, *407*, 83–87. [[CrossRef](#)]
68. Baccega, E.; Bottarelli, M.; Su, Y. Alternative Experimental Characterization of Phase Change Material Plasterboard Using Two-Step Temperature Ramping Technique. *Energy Build.* **2022**, *267*, 112153. [[CrossRef](#)]
69. Wijesuriya, S.; Tabares-Velasco, P.C.; Biswas, K.; Heim, D. Empirical Validation and Comparison of PCM Modeling Algorithms Commonly Used in Building Energy and Hygrothermal Software. *Build. Environ.* **2020**, *173*, 106750. [[CrossRef](#)]
70. Sun, V.; Asanakham, A.; Deethayat, T.; Kiatsiriroat, T. A New Method for Evaluating Nominal Operating Cell Temperature (NOCT) of Unglazed Photovoltaic Thermal Module. *Energy Rep.* **2020**, *6*, 1029–1042. [[CrossRef](#)]

Disclaimer/Publisher's Note: The statements, opinions and data contained in all publications are solely those of the individual author(s) and contributor(s) and not of MDPI and/or the editor(s). MDPI and/or the editor(s) disclaim responsibility for any injury to people or property resulting from any ideas, methods, instructions or products referred to in the content.